Acoustic plate-valve resonator for low-frequency sound absorption

Md Robiul Hossain (ID) ; Eoghan P. Ross (ID) ; Gareth J. Bennett ✉ (ID)

Check for updates

CrossMark

View Online   Export Citation

Articles You May Be Interested In

Piezomodulated Raman spectroscopy of molecular crystals: An experimental method for study of the anharmonic properties of solids
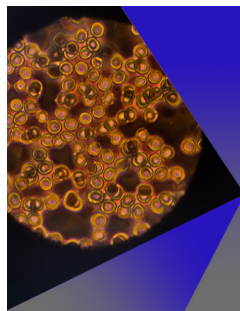
J. Chem. Phys. (February 1985)

Multi-agent cooperation rescue algorithm based on influence degree and state prediction

AIP Conference Proceedings (April 2018)

Effects of oxygenated additives and Al_2O_3-TiO_2 thermal\barrier piston coating on diesel engine fueled with non-edible biodiesel

AIP Conference Proceedings (October 2019)

Acoustic plate-valve resonator for low-frequency sound absorption

View Online   Export Citation   CrossMark

Md Robiul Hossain, [ID] Eoghan P. Ross, [ID] and Gareth J. Bennett[a] [ID]

AFFILIATIONS

Trinity College Dublin, The University of Dublin, Dublin D02 PN40, Ireland

[a]Author to whom correspondence should be addressed: gareth.bennett@tcd.ie

ABSTRACT

An acoustic plate-valve resonator is developed and optimized to maximize absorption by enhancing the Helmholtz resonance with coincident structural vibrations of the plate-valve. The current research initially examines the concept experimentally with a 3D printed valve. Then with the use of analytical and numerical modeling, a structural analysis is performed, which allows the eigenmodes and eigenfrequencies of the plate-valve to be determined. When the resonator properties are modified by changing either the depth of the backing cavity or the thickness of the plate-valve, the system can be designed in such a way that the Helmholtz resonance can be coincident with a particular eigenfrequency, leading to absorption higher than that achieved in the absence of such a flexible plate-valve. In addition, absorption also occurs at frequencies other than the Helmholtz frequency due to the vibration of the plate at additional eigenfrequencies. Both of these aspects of the technology advance the state-of-the-art in Helmholtz resonator design. Good agreement has been found between the modeling and experimental results. Near-perfect absorption was achieved experimentally, e.g., up to $\alpha = 0.995$ below 1 kHz; in addition, given that the thickness of the technology can be a very small percentage of the acoustic wavelength that it is absorbing, deep sub-wavelength ratio absorbers can be designed, e.g., a ratio of up to 58 was achieved in this study with a 5 mm deep technology at 1.18 kHz.

I. INTRODUCTION

Noise is an alarming concern due to its harmful effects on the environment, health, and the quality of human life. Growing urban population leads to growth in the construction of buildings and private or public transportation systems. The aviation industry has also seen dramatic growth over the last 20 years, with passenger numbers increasing from 1.5×10^9 in 1998 to 4×10^9 in 2017. People who live in the vicinity of major airports experience considerable amounts of sound pollution. Exposure to loud noise increases the risk of developing several adverse health conditions such as high blood pressure, hypertension, fatigue, stress, coronary heart diseases, etc.[1] Sleep disturbance due to noise pollution also leads to reduced work and school performance, hence making it vital to eliminate this undesired noise.

Traditional natural porous materials such as wool and cotton as well as synthetic glass fiber and melamine foams have been used for noise reduction for many years. However, these materials are effective only at reducing high-frequency noise at reasonable thicknesses. According to the mass density law, a thicker porous material is required to attenuate low-frequency noise. Adding mass and increasing thicknesses (which can equate to reducing useful space) are to be avoided in the construction of buildings and factories where people can be exposed to noise. With regard to transportation noise, both weight and space are critical parameters, which need to be minimized in order to reduce fuel consumption and the associated environmental cost.[2,3] Although composite structures such as perforated absorbers, acoustic mufflers, double walls with cladding, etc., have been used in rooms, auditoriums, offices, aircraft fuselages, cars, trains, etc., to attenuate low-frequency noise, the attenuation of low-frequency noise in a thin form factor still remains an intractable challenge.

Since the early 2000s, research in the field of acoustic metamaterials (AMMs) has expanded considerably with respect to the application of low-frequency noise reduction. Originating in the fields of electromagnetics and optics, the extension of research to acoustic metamaterials has led to this nascent research activity in acoustics, which has tremendous potential for the development

of fundamental science and for revolutionary technological breakthroughs. Acoustic metamaterials are artificial structures that are periodic in nature and that often involve local resonators designed to resonate at specific frequencies, rendering them, therefore, often tonal or highly narrow band in nature.

Traditionally, micro-perforated panel absorbers (MPPA) have been used for broadband sound absorption, but these typically only work in mid- to high-frequency ranges. Some AMM research has been reported for low-frequency sound absorption. Mei et al.[4] demonstrated a membrane plate system for low-frequency absorption as low as 164 Hz. Subsequently, Li et al.[5] proposed a metasurface-based structure that can absorb the incident acoustic energy at a low-frequency of around 125 Hz. Their structures are composed of a perforated plate and a labyrinthine structure. They also presented extremely low-frequency absorption (around 50 Hz) with a multi-coiled metasurface[6] and broadband sound absorption in the frequency ranges of 460–972 Hz and 232–494 Hz with supercell-based acoustic metasurface coiled absorbers.[7] Lee et al.,[8] Wang et al.,[9] Temiz et al.,[10] and Martincic et al.[11] studied the MPP-based low-frequency absorber including the vibro-acoustic and panel vibration effect of the structure. McKay et al.[12] very successfully developed a novel low-frequency broadband sound absorber, called a SeMSA, by combining decorated membranes and micro-perforated plates, and Davis et al.[13] used graph theory based on a two point impedance method to optimize a multi-chamber SeMSA, which resulted in a very broadband low-frequency absorption response or even an absorption response tailored for fan noise. Killeen et al.[14] applied the SeMSA to reduce the fan-noise of data-center telecommunications' server racks, which is particularly challenging as it is a grazing acoustic and grazing flow boundary condition. Wang and Bennett[15] applied the two point impedance method to optimize a multi-chamber MPPA, which has resulted in a very broadband low frequency absorber.

In the literature, AMMs typically comprised an inhomogeneous technology where components are directly connected to one another. Some exceptions to this are cited here where the motion of a cantilever beam absorbs sound through the resultant micro-slits. Farooqui and Aurégan[16] and D'elia et al.[17] proposed a numerical and analytical model for a structure composed of a flexible cantilever beam producing acoustic micro-slits with a compact cavity and demonstrating attenuation around 500 Hz with a 3 cm cavity depth. Aurégan and Farooqui[18] developed a sub-wavelength acoustic absorber using an MPP-based thin flexible beam with micro-slits for perfect sound absorption in the mid-frequency range.

In the current work, the concept of an acoustic plate-valve design has been developed based on the promising preliminary investigations of off-the-shelf elastomeric valves,[19] which are used as one-way valves in fluidic-control. As is well understood, the standard Helmholtz resonator consists of a rigid volume with an orifice, which is stationary. In this work, a Helmholtz resonator has been developed, which has an unusual plate-valve located at the opening. The plate-valve is flexible with the capacity to vibrate at its natural frequencies. When the resonator properties are modified by either changing the depth of the backing cavity or the thickness of the plate-valve, the system can be designed in such a way that the Helmholtz resonance can be coincident with a particular eigenfrequency, leading to absorption higher than that achieved in the absence of such a flexible plate-valve.

II. ACOUSTIC PLATE-VALVE METAMATERIAL DESIGN AND FABRICATION

Further to the work of Bennett et al.[19] discussed in the introduction, testing has been performed using 3D printed valves similar to one of the original elastomeric umbrella valves[19] but of a much larger diameter, ϕ_{APV} = 124 mm, with a thickness of t_{APV} = 0.5 mm, as shown in Fig. 1. The diameter of 124 mm was chosen to maximize the size of the plate-valve when measured in a cylindrical impedance tube of 127 mm diameter, but by allowing for a gap of 1.5 mm between the outer diameter of the plate-valve and the inner diameter of the tube, local edge viscous losses are minimized, focusing the attention of the study on the interaction between the plate-valve and the mounting plate.

This one-way valve was manufactured with an Ultimaker-3 FDM 3D printer using a print layer resolution of 0.15 mm. The Ultimaker-3 was chosen as it has two printer heads, which enable printing with two different materials at the same time. In this case, a polylactic acid (PLA) was chosen as the main material of the plate-valve while water-soluble polyvinyl alcohol (PVA) was used as the support scaffolding. By using a water-soluble PVA, the scaffolding is more easily and completely removed, resulting in a more accurate shape and a better surface finish.

Figure 2 shows the one-way valve examined in this current research along with its mounting plate. The mounting plate was manufactured using aluminum and is 5.8 mm thick. Similar to the spacer plates used in the impedance tube, see Fig. 14, it is square, 200 × 200 mm², and designed to have a sliding fit inside the square test section. Its hole is designed to provide maximum open area while allowing an overlap of 8 mm with the plate-valve, see Fig. 1(c). Due to the need to mount the plate-valve on the plate, two narrow ribs are required, so the opening is not complete, see Fig. 2(d). The plate-valve was designed with a central strut, which allows for a simple push-and-twist installation process into the mounting plate. The length of the strut was designed in such a way that the plate-valve is in contact with the mounting plate around its perimeter once installed.
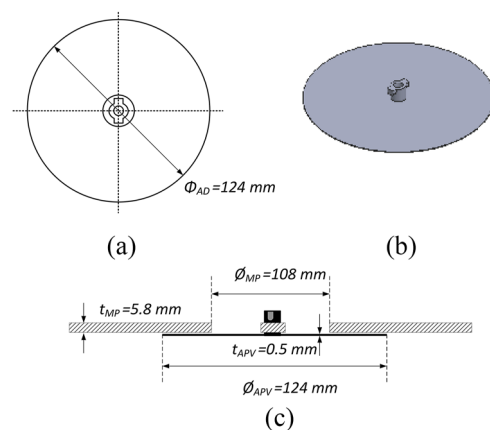

FIG. 1. Nominal geometric parameters of the acoustic plate-valve. (a) Plan view. (b) CAD design. (c) Elevation view.
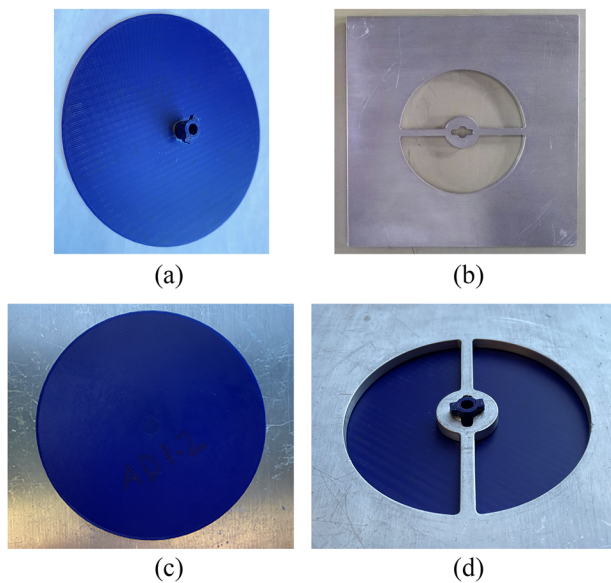
FIG. 2. 3D printed acoustic plate-valve sample and the mounting plate. (a) 3D printed acoustic plate-valve sample. (b) Mounting plate for acoustic plate-valve. (c) Mounted 3D printed acoustic plate-valve sample (Top view). (d) Mounted 3D printed acoustic plate-valve smaple (Bottom view)

Although the designed thickness of the valve was 0.5 mm, the printed sample had a slightly non-uniform thickness over the surface area. The average thickness was measured to be 0.52 mm using a micrometer calipers. The value of 0.52 mm was subsequently used for the numerical and analytical analysis.

III. RESULTS AND DISCUSSION

In this section, analytical, experimental, and numerical results are presented as a function of the cavity depth, material properties, and plate thickness.

Figure 3 provides some initial baseline results. The absorption coefficient was measured experimentally for an empty tube, and then with the mounting plate installed but without the acoustic plate-valve, see Fig. 2(b). In both cases, there was a 40 mm cavity depth. The empty tube, as expected, results in effectively zero absorption (full reflection), demonstrating the correct functioning of the rig and methods. The frequency domain numerical solution provides an identical result, demonstrating the correct functioning of the numerical model. When the mounting plate is inserted, it results in non-zero absorption, with the numerical and experimental results in close agreement. Some losses are assumed to occur due to acoustic velocity flow around the edges of the mounting plate, but as the value of absorption is less than 0.1 in the frequency range, it is assumed from here on that the mounting plate itself has little effect on the absorption coefficient.

Figure 4 shows the absorption coefficient when the acoustic plate-valve is inserted with a very shallow 5 mm cavity depth. The numerical result shows two relatively wideband peaks with very high absorption coefficients, the first being at 1140 Hz and the second at 1460 Hz. The experimental result is again in very close agreement with a slight frequency shift at the lower frequency, but also to be noted are indications of other peaks not found in the numerical result. This will be discussed further in the paper. A very significant result for this configuration is that the lower frequency peak has perfect absorption experimentally at a cavity depth of only 5 mm. This means for a frequency of 1184 Hz, which has a wavelength of 0.29 m, the acoustic plate-valve technology is deeply sub-wavelength with perfect absorption at a depth-to-wavelength ratio of 58.

Figure 5 shows the comparison of the experimental and numerical absorption coefficients for the acoustic plate-valve with differing cavity depths: 10, 20, 30, and 40 mm. The absorption coefficient for the numerical main peaks seems to monotonically decrease whereas for the experimental results, the absorption coefficient is higher for the 40 mm cavity depth than for the 30 mm cavity depth. This point will also be further investigated in the paper. Examining the general results for the absorption coefficient for the acoustic plate-valves now, we see that the results are extremely good, with the numerical
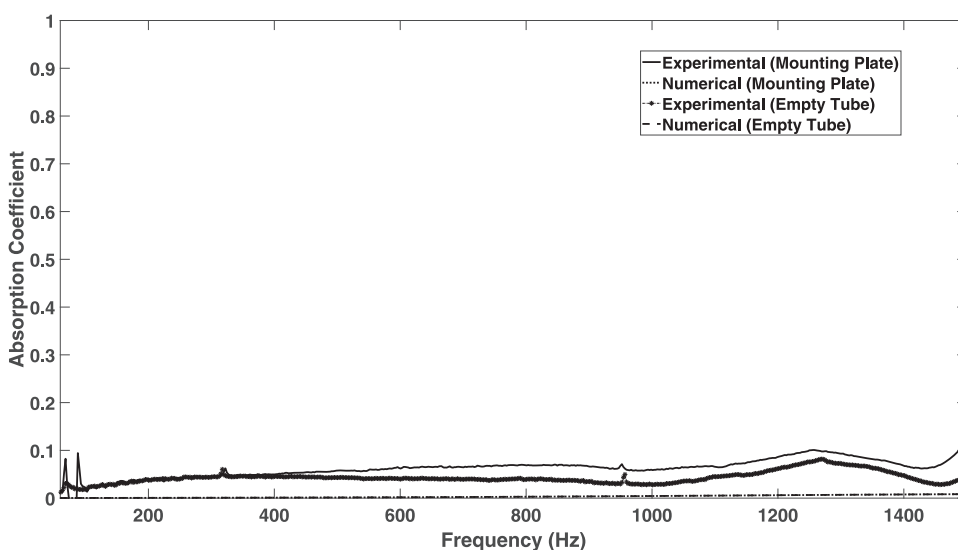

FIG. 3. Absorption coefficient for the mounting plate only with no acoustic plate-valve. 40 mm cavity depth.
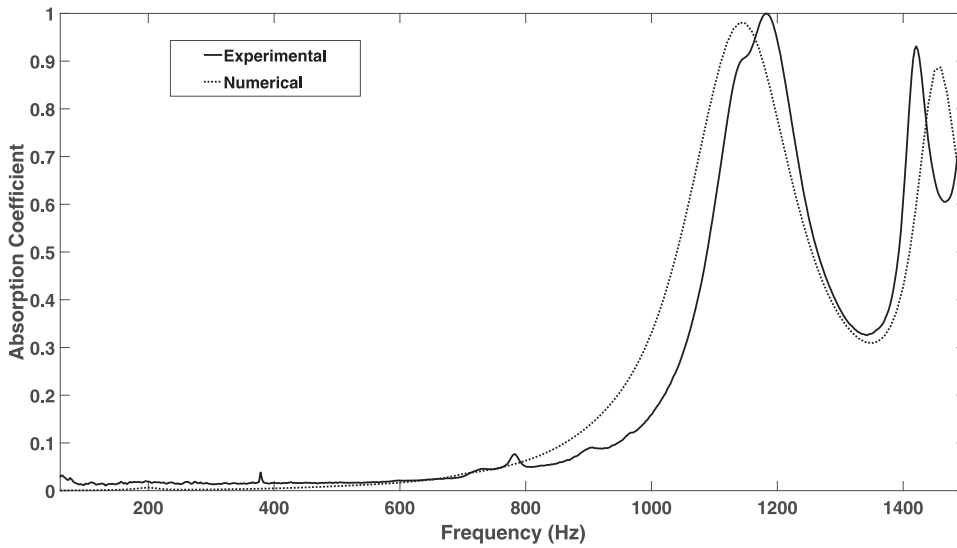
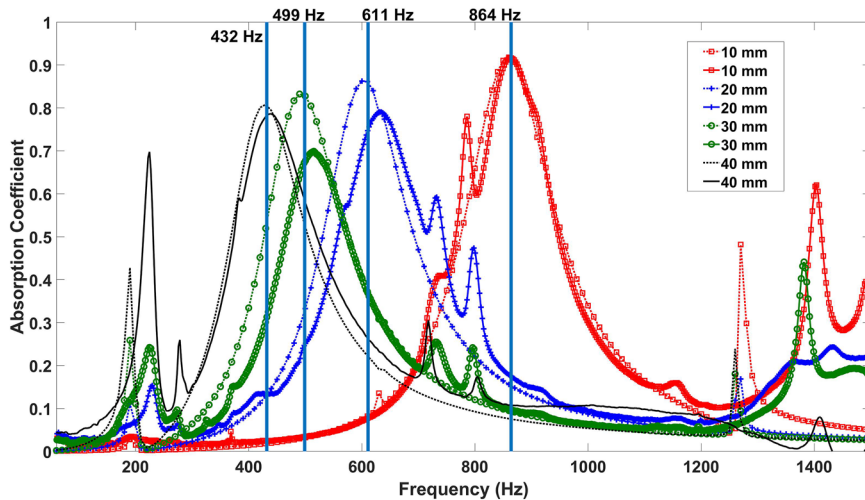**FIG. 4.** Absorption coefficient for 5 mm cavity depth.

FIG. 5. Absorption coefficient for 10, 20, 30, and 40 mm cavity depths. Solid line: experimental. Dotted line: numerical.

and experimental results agreeing well with each other. By increasing the depth of the cavity, lower frequencies can be attenuated, and although the magnitude of absorption decreases with frequency, it remains quite high.

A. Helmholtz resonance of the acoustic plate-valve metasurface

With regard to the frequency at which the main peak occurs in Fig. 5, there seems to be a non-linear relationship between the depth and the frequency. This behavior allows us to identify the main peak as resulting from a Helmholtz resonance. Through observation of the standard Helmholtz equation,

$$f_{HR} = \frac{c_0}{2\pi} \sqrt{\frac{S_n}{L_n V_c}}, \tag{1}$$

where L_n and S_n are the neck's effective length and area, respectively, and V_c is the effective cavity volume, we can see that when the depth of the back-cavity is doubled, the frequency of the main peak decreases by $\frac{1}{\sqrt{2}}$. The frequencies of peak absorption from the numerical analysis shown in Fig. 5 are 860, 600, 490, and 430 Hz. As an example, 600 Hz is very close to $\frac{860}{\sqrt{2}}$, and 430 Hz is very close to $\frac{600}{\sqrt{2}}$; it is reasonable to deduce that these main peaks result from a Helmholtz resonance where the neck is the circumferential gap between the plate-valve and the mounting plate. Unlike typical Helmholtz resonators, the orifice here is not a single hole whose axis is parallel to that of the cavity, but rather it is a circular gap whose axis is perpendicular. In addition, due to the fact that the plate-valve vibrates, which causes the gap to change over time and is a function of radius, the geometry of the neck is less straightforward to determine.

To try and understand the underlying mechanism of Helmholtz resonance in the acoustic plate-valve configuration, the geometry is
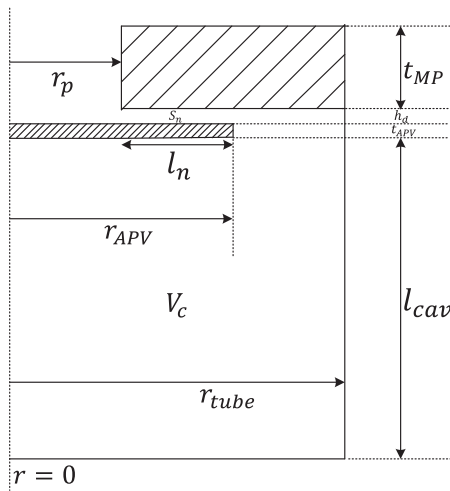
FIG. 6. Axisymmetric schematic of the acoustic plate-valve and cavity.

TABLE I. Parameters and values of the terms shown in Fig. 6.

Geometric parameter	Symbol	Value (mm)
Mounting plate hole radius	r_p	54
Acoustic plate-valve radius	r_{APV}	62
Impedance tube inner radius	r_{tube}	63.5
Neck nominal length	l_n	8
Mounting plate thickness	t_{MP}	5.8
Nominal gap	h_d	0.4
Plate thickness	t_{APV}	0.52
Cavity depth	l_{cav}	5–40

examined as shown in Fig. 6, which is considered to be axisymmetric around its axis at $r = 0$. This assumption ignores the effect, if any, of the presence of the mounting plate ribs, as seen in Fig. 2(b). The definition and value of the terms are provided in Table I.

The nominal neck length is considered to be the overlap of the plate-valve over the mounting plate, l_n, and the volume of the cavity,

V_c, is straightforward to calculate. However, the area of the neck is complicated by the fact that the radius at the beginning of the neck, r_p, is different from that at its end, r_{APV}. A reasonable approximation is to calculate the area as $2\pi r_{av} h_d$, where $r_{av} = (r_p + r_{APV})/2$. Using these values and the same value for the air gap as used in the numerical analysis (see Appendix A 2), $h_d = 0.4$ mm, the analytical results calculated using Eq. (1) are compared to those calculated by the experiments and the numerical analysis and are shown in Table II. However, it can be seen that the analytical results shown in column 4 underestimate both the experimental and numerical values.

To gain further insight, an additional numerical analysis of the system was performed, but in this case, the plate valve was held fixed and rigid and was not allow to vibrate. For the initial analysis, where the same value of the air gap is used for the rigid plate, $h_d = 0.4$ mm, the Helmholtz frequencies were significantly different. This highlights the fact that the physics of the systems with flexible and rigid plates are different. The analysis was then repeated until a gap was found, which gave the same Helmholtz peak frequencies as for the flexible plate case. These values are tabulated in column 5 of Table II, and the absorption curve spectra are provided in Fig. 7. The gap value, which provided the same Helmholtz peak frequencies, was found to be much greater at $h_d = 1.3$ mm. The observation here is that a flexible plate valve behaves as a rigid plate resonator with a larger gap but only from a Helmholtz frequency perspective. It can be observed that the absorption magnitudes of the flexible acoustic plate-valve resonator are greater at the Helmholtz peak frequencies. In addition, the additional high absorption peaks seen in Fig. 5 are not present when the plate valve is rigid. Both of these facts demonstrate the benefit of making the plate flexible.

Furthermore, the acoustic particle velocity in the vicinity of the air gap was examined for the rigid plate case. An example of this is provided in Fig. 8. It is clear in this figure that the viscous boundary layer is not confined to the air gap alone, but, as is commonly observed in ducts, effects continue into the field at both ends. This implies that end corrections to the term l_n as a function of gap size must be implemented into the analytical analysis. Once the effective length of the neck is increased to accommodate for the end corrections, we see in column 6 of Table II that the same peak frequencies can be correctly modeled.

Further research must be undertaken to determine a means to estimate the effective average gap, but in this study, it seems clear that the principal absorption peak that varies with the cavity depth is due to Helmholtz resonance.

TABLE II. Helmholtz frequencies as a function of backing cavity depths.

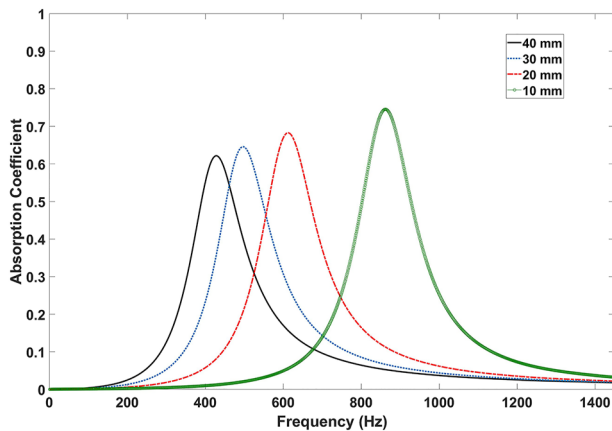| Cavity depth l_{cav} (mm)	Experimental *flex.* f_{HR} (Hz)	Numerical *flex.* ($h_d = 0.4$ mm) f_{HR} (Hz)	Analytical *flex.* ($h_d = 0.4$ mm) f_{HR} (Hz)	Numerical *rigid* ($h_d = 1.3$ mm) f_{HR} (Hz)	Analytical *rigid end correction* ($h_d = 1.3$ mm)
40	439	430	328	427	432
30	515	490	379	496	499
20	634	600	465	613	611
10	861	860	657	861	864

FIG. 7. Absorption coefficient for 10, 20, 30, and 40 mm cavity depths. Numerical solution for a rigid plate that does not vibrate. h_d = 1.3 mm.
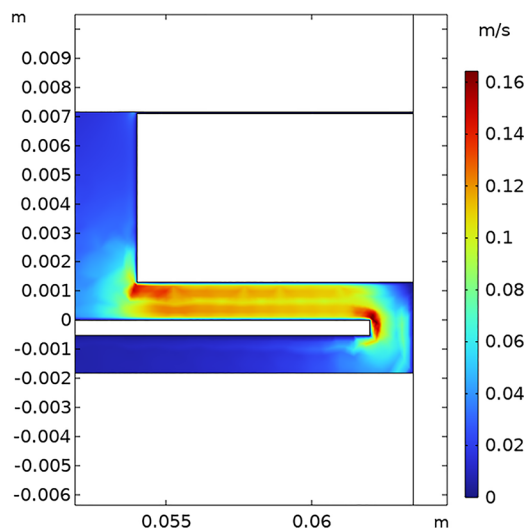

FIG. 8. Particle velocity in the vicinity of the air gap from a 2D axisymmetric FEM simulation. Numerical solution for a rigid plate that does not vibrate. l_{cav} = 40 mm; h_d = 1.3 mm.
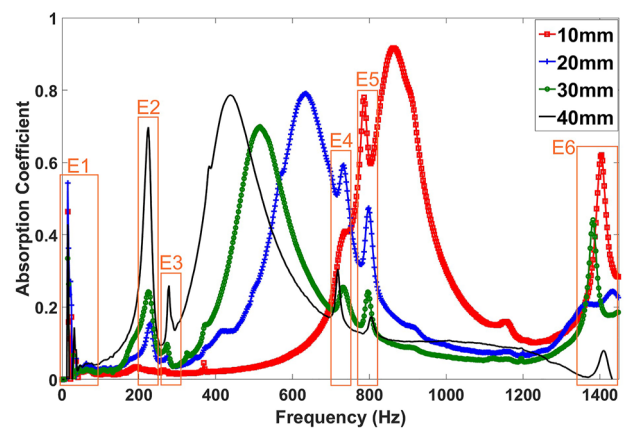
B. Vibrational analysis of the acoustic plate-valve

In Fig. 5, we saw high absorption from the acoustic plate-valve at the Helmholtz frequency and good agreement between experimental and numerical results in the Helmholtz frequency range for the 10 and 40 mm cavity depths. There are small discrepancies in amplitude and frequency for the 20 and 30 mm deep cavities.

In addition to the acoustic plate-valve providing high absorption at the Helmholtz frequencies, we can also see absorption peaks at other frequencies. Figure 9 separates out Fig. 5 into the numerical and experimental results for clarity. In Fig. 9(a), it is clear that there are three frequency ranges—N1, N2, and N3—where for each of the cavity depths, there are absorption peaks that do not vary with depth. These are considered to be associated with structural
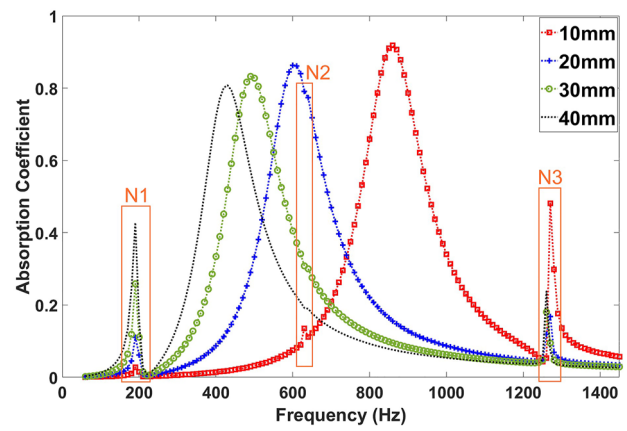
(a)

(b)

FIG. 9. Acoustic plate-valve absorption results as a function of cavity depth. (a) Numerical results. (b) Experimental results.

vibrational modes of the flexible acoustic plate-valve whose frequencies are more a function of material properties than of cavity depth. The peaks in the N2 range tend to be masked by the Helmholtz curves, whereas for the N1 and N3 frequency ranges, the peaks increase in magnitude as the Helmholtz peaks approach them in frequency.

In Fig. 9(b), we see that in the experimental results, additional absorption peaks associated with vibrational modes are present. This can be explained by the fact that the frequency domain numerical solution is an axisymmetric analysis, and thus, only radial nodes for the axisymmetric zeroth azimuthal mode, i.e., $A_{(m,n)} = A_{(0,n)}$, can be resolved. For the inherently 3D experimental results, as can be assumed at this point, all vibrational modes can be excited to different degrees of amplitude response.

It is clear that, while there is a similarity in frequency between the vibrational peaks in both the experimental and numerical results, the exact frequencies and amplitudes are not the same. A short study was conducted, as shown in Fig. 10, where the material properties of the PLA were altered from the values used. The values of ρ, E, ν, and η were varied for l_{cav} = 40 mm to ρ = 1240 kg m^{-3}, $E = 3.8 \times 10^9$ Pa,
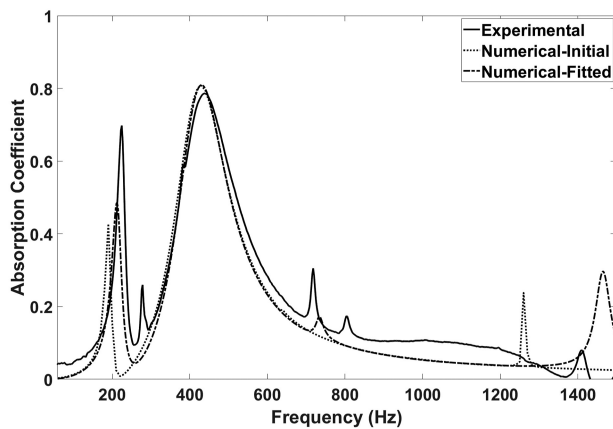
FIG. 10. Comparison of the absorption response when the material properties in the numerical model are altered. 40 mm cavity depth.

TABLE III. Eigenfrequencies of a completely free thin circular plate in vacuum.

Analytical f_{0n} (Hz)	Numerical eigenfrequency analysis f_{0n} (Hz)
94.4	94.2
400.5	399.9
912	912
1631	1628

$\nu = 0.33$, and $\eta = 0.03$ as opposed to the results shown in Appendix A 2. Through observation of Fig. 10, it can be seen that the vibrational peaks are sensitive to these material property parameters whereas the Helmholtz frequency remains unchanged. The frequencies and amplitudes have increased, and a peak at ~750 Hz has now appeared where there was none before.

Referring back to Fig. 9, it is plausible to think that the numerical peaks at N1 correspond to either E2 or E3, those at N2 correspond to either E4 or E5, and those at N3 correspond to E6.

1. Analytical and numerical eigenfrequency analysis

To gain further insight into the nature of the vibrational modes responsible for these absorption peaks, analytical models from the literature have been examined. For analytical modeling, the acoustic plate-valve can be considered as a thin circular plate. The eigenfrequencies of a thin circular plate ($t_{APV} \ll r_{APV}$) are given by Chiang and Huang[20] in the following equation:

$$f_{mn} = \frac{\lambda_{mn}^2}{2\pi r_{APV}^2} \sqrt{\frac{D}{\rho t_{APV}}}, \tag{2}$$

with

$$D = \frac{E t_{APV}^3}{12(1 - \nu^2)}, \tag{3}$$

where D is the flexural rigidity. The parameter λ_{mn} can vary to represent the eigenvalues of specific particular boundary conditions (e.g., free, clamped all around, simply supported, centrally clamped free edge, etc.). The calculated eigenvalues for different boundary conditions for a thin plate are provided by Timoshenko et al.,[21] Southwell,[22] and Colwell and Hardy[23] and are well documented by Leissa.[24] For example, if we consider the symmetric mode $A_{(m,n)}$ where $m = 0$, $n = 1,2,3 \ldots$, and $\nu = 0.33$ for a completely free plate, the analytical eigenvalues are calculated to be $\lambda_{0n} = 3.014, 6.209, 9.370, 12.53, \ldots$.[24] Table III shows the first four analytical eigenfrequencies of a completely free thin circular plate.

In addition, a vibrational (eigenfrequency) analysis of the same free thin circular plate was conducted in COMSOL. The medium is vacuum to match that in the analytical model. The numerical and analytical eigenfrequencies are well matched and validate each other as models.

For the acoustic plate-valve attached to the experimental rig, it can be considered as a thin circular plate free at the edge but fixed at the center. Southwell[22] solved the problem with a free circular disk clamped at the center as an annulus plate free on the outside and clamped on the inner edge, which is well suited for the current configuration of the acoustic plate-valve. The first column of Table IV shows the eigenfrequencies (in a vacuum) from the analytical model of the acoustic plate-valve modeled as a centrally fixed free edge thin plate.[24]

The simulated eigenfrequencies and mode shapes of the acoustic plate-valve from the COMSOL eigenfrequency analysis are shown in Table V, and the numerically determined eigenfrequencies are also tabulated in the second column of Table IV. Although the FEM simulation is based on a 2D axisymmetric model, the 3D mode shapes of the acoustic plate-valve were generated using post-processing of the 2D results for better visualization. The eigenfrequency analysis in vacuum for this simplified boundary condition allows for this 3D prediction, whereas the full frequency domain COMSOL numerical analysis in Appendix A 2, as shown in Fig. 9(a), for example, does not. First of all, by reviewing the first two columns of Table IV, we see that the analytical results compare extremely well with the eigenfrequency numerical analysis. Looking at the mode shapes in Table V, we see the azimuthal and radial mode shapes and their combinations, providing us with a valuable understanding of the vibration of the acoustic plate-valve. By comparing these frequencies with those of the non-Helmholtz frequency peaks to be found in the experimental and frequency domain numerical results in Fig. 9, we can verify that these are indeed due to excited natural vibrations in the acoustic plate-valve, as postulated.

Referring to Fig. 9(a) initially, it seems clear that the peaks to be found in frequency ranges N1, N2, and N3 correspond to $A_{(m,n)} = A_{(0,1)}, A_{(0,2)}, A_{(0,3)}$, which are radial modes with no azimuthal modes present. When these frequencies are entered into column four in Table IV, we see that, although the frequencies themselves are not exactly precise, the difference can be explained by the fact that the analysis was performed in air and not vacuum and that the full impedance tube assembly including the mounting plate, tube, and back cavity was included in the model and also by the issues related to uncertain material properties.

Referring now to Fig. 9(b), we conclude that the many additional non-Helmholtz frequency peaks can be attributed to acoustic

TABLE IV. Modal frequency comparison.

| Mode (m, n) | Fundamental natural frequency f_{mn} (Hz) | | | |
	Analytical	Numerical (eigenfrequency)	Experimental	Numerical (frequency domain)
(0,0)	43	43	E1	
(0,1)	240	242	E2	N1
(0,2)	703	698	E4	N2
(0,3)	1384	1378	E6	N3
(1,0)	⋯	14	E1	
(1,1)	236	245	E3	
(1,2)	687	705	E5	
(1,3)	1366	1392	E6	
(2,0)	60	61	•	
(2,1)	405	406	•	
(2,2)	963	972	⋯	
(3,0)	140	141	⋯	
(3,1)	607	609	⋯	
(3,2)	1278	1288	•	

plate-valve natural frequencies being excited by the white noise in the impedance tube. Not all theoretical modes are easily identifiable in the experimental data, and their amplitude response varies both as a function of frequency and cavity depth, but it is possible to make reasonable assumptions with regard to many of the modes. Frequency ranges E1-E6 contain cavity depth independent absorption peaks, which do correspond reasonably with the theoretically predicted vibrational modes. This can be seen in Table IV in column four where E1-E6 have been entered. Experimental peaks with low amplitude have also been represented but with a bullet point in the table, indicating that these modes seem to have been experimentally excited but with a low amplitude response. Once again, where frequencies are lower than those derived in vacuum, the added mass effect of the air can be used as an explanation.[25–34]

The analysis in Tables IV and V allows us to explain the presence of the additional peaks in Fig. 9 and to visualize them.

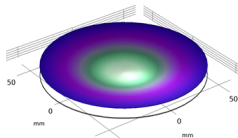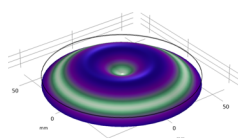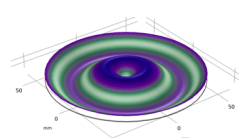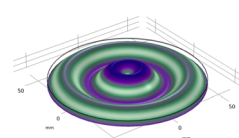## C. Particle velocity in the acoustic plate-valve neck/gap
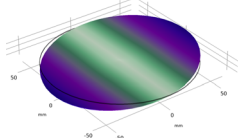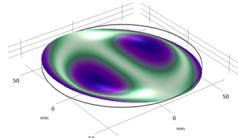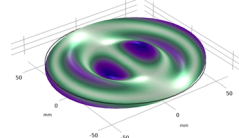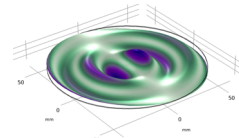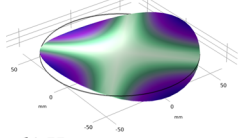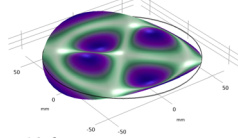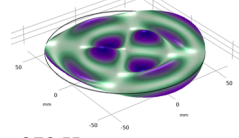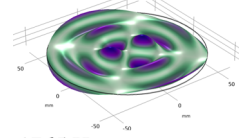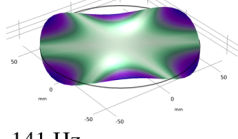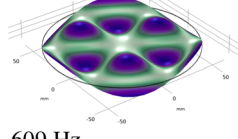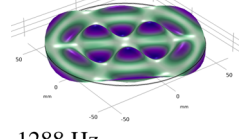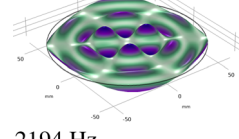
The particle velocity profile in the air gap, $h_d = 0.4$ mm, between the mounting plate and acoustic plate-valve (neck of the Helmholtz resonator) was calculated using the frequency domain numerical model for the 40 mm depth cavity, and the results are shown in Fig. 11. The three radial mode peaks $A_{(m,n)} = A_{(0,1)}$, $A_{(0,2)}, A_{(0,3)}$ and the Helmholtz resonance peak were examined for the fitted numerical case in Fig. 10. A viscous boundary layer formation can be observed in each of the plots. Figure 11(b) shows the velocity profile for the Helmholtz resonance, and not only does it have the highest particle velocity but it is also the only frequency for which uniform velocity along the full length of the neck is found. This proves that Helmholtz resonance is the result of the compressibility effect with the entire slug of air in the neck oscillating
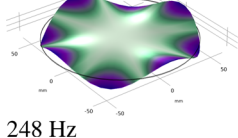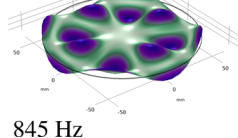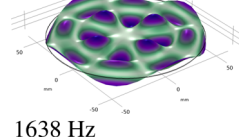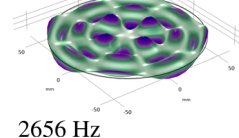
harmonically. The maximum point velocity in Fig. 11(a) is also high,, but as it is not as distributed as that for the Helmholtz resonance case, it makes sense that its peak in Fig. 10 is not that high. The velocity distribution for the three radial modes, unlike that for the Helmholtz resonance frequency, shown in Fig. 11(b), is not uniform, presumably being influenced by the fluctuation of the flexible plate-valve.

D. Structural-Helmholtz resonance coincidence

In Fig. 9 we observed that, as with micro-perforated panel absorbers, there is not only a decrease in the frequency of the Helmholtz resonance with increasing cavity depth but also a decrease in the magnitude of absorption. As has been noted, in the experimental results, the decrease in amplitude does not monotonically decrease with frequency. Given that there are additional vibrational modes with significantly high absorption peaks in that frequency range, an investigation was conducted to determine whether a frequency coincidence between the structural and Helmholtz resonance frequencies could influence the amplitude response. From observation of Fig. 9(b), it can be seen that there are two dominant structural resonances in the frequency range between the Helmholtz resonance peaks when the cavity depths are 10 and 20 mm, i.e., E4 and E5, which possibly correspond to the $A_{(0,2)}$ and $A_{(1,2)}$ modes. By varying the cavity depth more precisely, it is possible to adjust the frequency of the Helmholtz resonance peak so that it coincides with one of these structural resonance frequencies. In Fig. 12, we see the result of the investigation. By using Eq. (1), it is possible to predict the Helmholtz resonance frequency as a function of cavity depth. Figure 12 shows the result for three cavity depths between 10 and 20 mm, i.e., at 12, 13, and 14 mm. The 14 mm cavity depth aligns the Helmholtz frequency well with the $A_{(0,2)}$ mode and results in near-perfect absorption ($\alpha = 0.995$) at the coincident

TABLE V. Eigenfrequencies and the corresponding mode shape from the 2D axis-symmetric numerical model for the centrally fixed free edge circular plate: eigenfrequency analysis.

$m \Downarrow \diagdown \ n \Rightarrow$	0	1	2	3
0	44 Hz	242 Hz	698 Hz	1378 Hz
1	14 Hz	245 Hz	705 Hz	1392 Hz
2	61 Hz	406 Hz	972 Hz	1765 Hz
3	141 Hz	609 Hz	1288 Hz	2194 Hz
4	248 Hz	845 Hz	1638 Hz	2656 Hz

frequency. Similarly, the 12 mm cavity aligns the Helmholtz resonance, perhaps, not quite as well with the $A_{(1,2)}$ mode, resulting in a very high absorption coefficient ($\alpha = 0.97$), which is certainly higher than that of the original 10 mm cavity depth. The 13 mm cavity depth has the Helmholtz resonance in between the two structural resonances, and it can be seen that it and the structural resonance magnitudes are all higher than that when the cavity depth is 20 mm, for example.

E. Effect of thickness

In Sec. III D, it was seen that it is possible to attain coincidence by adjusting the cavity depth so that its Helmholtz frequency changes to that of the structural resonance frequency. Similarly, it should be possible to adjust the properties of the acoustic plate-valve itself so that a structural eigenfrequency can be changed to match the Helmholtz frequency. We saw in Fig. 10 that changing the material properties such as the values of ρ, E, v, and η results in structural resonant mode alteration without affecting the Helmholtz frequency. A

change in the 3D printing filament from the PLA to say ABS would achieve this, but in order to minimize the number of parameters changed at any one time, the PLA was maintained, and instead the thickness of the plate-valve was increased. Through observation, it can be seen that by substituting D in Eq. (3) into Eq. (2), the relationship between the thickness of the thin circular plate and resonant frequency becomes directly proportional. It can be seen in Fig. 9(b), that the E2 structural resonance frequency for the 40 mm cavity depth is approximately half that of the 40 mm Helmholtz frequency. Figure 13 shows the experimental impedance tube result for the same design 3D printed acoustic plate-valve but whose thickness is now 1 mm. Its absorption coefficient is superimposed on the original 0.52 mm thickness curve. The result is very satisfactory with the new coincident absorption response at 440 Hz increasing from ($\alpha = 0.79$) to ($\alpha = 0.97$) when the structural resonance is designed to align with the Helmholtz resonance. The cavity depth to wavelength ratio for 440 Hz is 20, demonstrating that deep subwavelength absorption can be achieved with almost perfect absorption at low frequencies such as this.

IV. CONCLUSIONS AND FUTURE RECOMMENDATIONS

The current research presents work to date on a novel acoustic resonator, which minimizes reflections from the walls of an enclosed space and thus absorbs sound. The technology employs the original idea of a flexible plate-valve applied to acoustics. Inspired by

off-the-shelf elastomeric fluidic one-way valves, acoustic plate-valves were 3D printed in a PLA to have a large diameter. The research demonstrates that the technology combines a Helmholtz resonator with structural vibrations in the plate, which themselves result in sound absorption for this small gap/air cavity configuration. It was shown that parameters such as the air

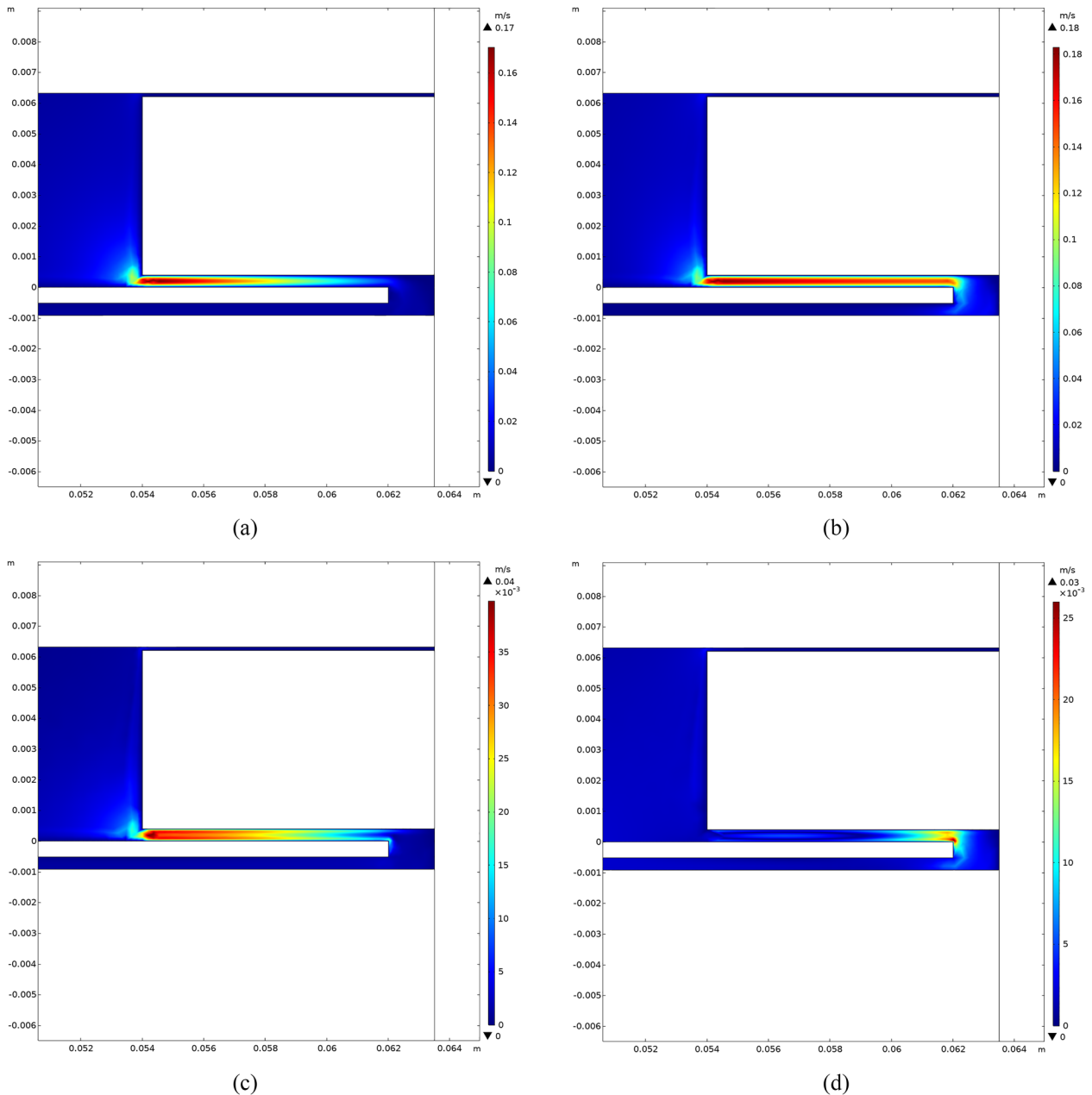**FIG. 11.** Distribution of the particle velocity from the 2D axisymmetric FEM simulation. Viscous boundary layer formation can be seen inside the air gap between the mounting plate and acoustic plate-valve. l_{cav} = 40 mm; h_d = 0.4 mm. (a) Total acoustic velocity at 212 Hz. (b) Total acoustic velocity at 430 Hz. (c) Total acoustic velocity at 735 Hz. (d) Toatl acoustic velocity at 1465 Hz.
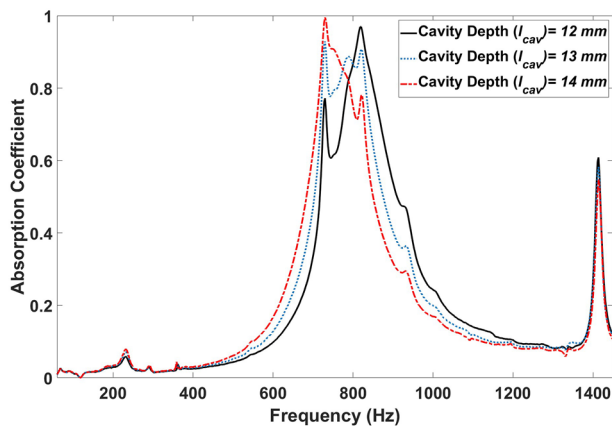
FIG. 12. Structural-Helmholtz resonance coincidence through varying the cavity depth.

FIG. 14. Impedance tube schematic.

cavity depth or the material properties of the plate-valve plate can be tailored at any required frequency so that resonant coincidence can be attained, which can result in near-perfect absorption (e.g., $\alpha = 0.995$), which is thus greater than what could be achieved by the Helmholtz resonator itself. Given that the thickness of the acoustic plate-valve plus the depth of the cavity can be a very small percentage of the acoustic wavelength that it is absorbing, deep subwavelength ratio absorbers can be designed, e.g., a ratio of up to 58 was achieved in this study. The technology presents the possibility for innovative acoustic absorbers for low-frequency noise attenuation in a thin profile. An FEM-based frequency domain modeling approach for the acoustic plate-valve has been validated to predict the acoustic performance. A simple 2D axisymmetric model has been implemented to reduce computational complexity and costs. The frequency domain model was compared with experimental results, which demonstrated strong agreement. An analytical model of the plate dynamics and a numerical eigenfrequency analysis allowed the natural frequencies to be calculated, and the latter allowed for visualization of the mode shapes. Future work will examine a fully 3D numerical model of the acoustic plate-valve, and a laser vibrometer-based measurement
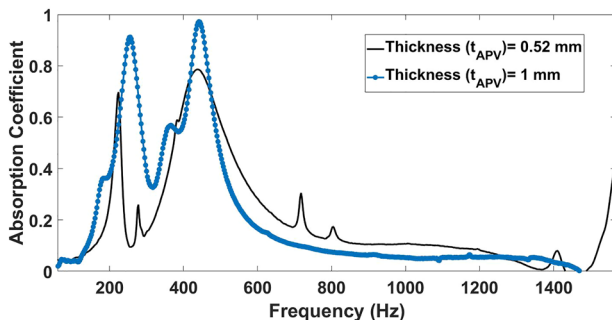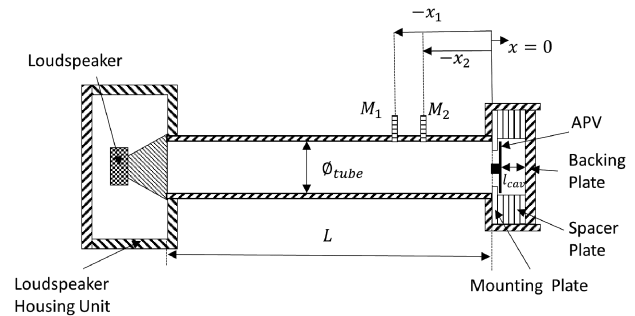
system will attempt to directly measure the mode shapes experimentally. A closer examination of the gap itself including viscous loss mechanisms and the case when the valve is fully closed due to negative pressure should also be investigated.

ACKNOWLEDGMENTS

AUTHOR DECLARATIONS

Conflict of Interest

The authors have no conflicts to disclose.

Author Contributions

M.R.H., E.P.R., and G.J.B. contributed equally to this work.

Md. Robiul Hossain: Conceptualization (equal); Data curation (equal); Formal analysis (equal); Investigation (equal); Methodology (equal); Software (equal); Validation (equal); Writing – original draft (equal). **Eoghan P. Ross**: Conceptualization (equal); Formal analysis (equal); Investigation (equal); Methodology (equal); Software (equal). **Gareth J. Bennett**: Conceptualization (lead); Data curation (lead); Formal analysis (equal); Funding acquisition (lead); Investigation (equal); Methodology (equal); Project administration (lead); Resources (lead); Software (equal); Supervision (lead); Validation (equal); Visualization (equal); Writing – original draft (lead); Writing – review & editing (lead).

DATA AVAILABILITY

The data that support the findings of this study are available from the corresponding author upon reasonable request.

APPENDIX A: METHODS

1. Experimental rig

Experimental measurement of the absorption coefficient was performed using the two-microphone impedance tube method. The

FIG. 13. Structural-Helmholtz resonance coincidence through varying the plate thickness.

tube was designed in accordance with the ISO standard 10534-2:2001[35] for impedance, reflection, and absorption measurements. A schematic of the experimental setup is shown in Fig. 14. The impedance tube, which was designed for high amplitude testing, is made of aluminum of 12.7 mm wall thickness, minimizing leakage and external noise ingress interfering with the data acquisition process. The tube has a circular cross section with an internal diameter of ϕ_{tube} = 0.127 m and therefore has a plane wave cut-off frequency of ~1.5 kHz. The tube has a length L = 0.78 m with the capacity to attach a second length of tube for sound transmission loss measurements in accordance with the ASTM standard E2611[36] although this is not investigated in this work. A high-amplitude loudspeaker is attached to the tube at one end. The loudspeaker used in this rig is a JBL 2206H/J 12 in. subwoofer. The frequency response of the subwoofer ranges from 45 Hz to 3.5 kHz, allowing for testing at low frequencies often not reproducible by smaller speakers and impedance tube rigs. The speaker is contained in a custom-built 18 mm thick plywood unit with a flange opening, allowing it to be mounted to the tube. A termination/test section to the tube was designed to allow for adjustable back-cavity depths. The termination is an aluminum, square section housing with a 24.75 mm wall thickness, which allows square spacer plates with circular holes of the same diameter as the internal diameter as the tube to be inserted behind the mounting plate, creating a back cavity. Spacer plates of different thicknesses can be combined to create a variety of back-cavity depths. A thick, 20 mm, solid aluminum backing plate with no holes was inserted downstream of the spacer plates to form the hard wall termination. Figure 15 shows a photo of the test setup with an additional solid hard wall backing bolted to the rear of the square test-section. Two G.R.A.S. 40 PH microphones (M_1 and M_2), with a frequency range of 20 Hz–20 kHz, were used in the rig and calibrated in accordance with the ISO 10534-2:2001[35] standard. The microphones were recessed into the wall of the impedance tube and were separated from the internal pressure field of the tube by a 2 mm diameter hole 1 mm in length. The microphones were located x_1 = 0.212 m and x_2 = 0.127 m from the face of the acoustic plate-valve mounting plate. The sample was tested using white noise with a sound pressure level (SPL) of 94 dB for 120 s. Other SPLs ranging from 100 to 120 dB were tested, but no significant non-linear effects were observed. The transfer function method was used in the analysis where the complex pressure reflection coefficient, r, is obtained from Cox and d'Antonio[37] as

$$r = \frac{H_{12}e^{jkx_1} - e^{jkx_2}}{e^{-jkx_2} - H_{12}e^{-jkx_1}}, \qquad (A1)$$

where $H_{12} = \frac{p(x_2)}{p(x_1)}$ is the transfer function between microphone positions and $k = \omega/c$ is the acoustic wave number. The absorption coefficient, α, is calculated from the reflection coefficient,

$$\alpha = 1 - |r|^2. \qquad (A2)$$

2. Numerical analysis

FEM simulations were performed using the commercial software COMSOL Multiphysics® version 5.6 with preset pressure acoustics, thermoviscous acoustics, and solid mechanics interfaces.

The acoustics module is well suited for all frequency-domain simulations with harmonic variations in the pressure field. A frequency domain analysis of the plane wave propagation has been performed where the acoustic plate-valve was modeled as a linear elastic material using the solid mechanics interface and the interior of the impedance tube was modeled as air with the pressure and thermoviscous acoustics interfaces. Coupling between thermoviscous acoustic and pressure acoustics is achieved with an acoustic-thermoviscous acoustic boundary while coupling between solid mechanics and thermoviscous acoustics is performed with a thermoviscous acoustic-structure boundary. The geometric parameters used in the simulation are chosen from the experimental setup described in Appendix A 1 with a variable cavity length (l_{cav}).

The geometric model for the FEM simulation, as shown in Fig. 16, is a simplified 2D axisymmetric model to reduce computational costs and time with little compromise of the fundamental characteristics. Sound-hard boundary walls and symmetry conditions are shown. The model represents the cylindrical impedance tube setup with the acoustic plate-valve, mounting plate, and back-cavity. The geometric coordinates for the plane in the 2D axisymmetric implementation are (r, z) and the angle φ is not defined since it is not a part of the computational domain implemented in the simplified model.

The material properties of PLA were taken from the literature:[38] mass density ρ = 1270 kg m^{-3}, Young's modulus E = 3.5 × 10^9 Pa, Poisson's ratio ν = 0.3,[39] and damping factor η = 0.025,[40] with typical values taken for air—mass density ρ_0 = 1.23 kg m^{-3}—and the speed of sound in air being c_0 = 343 m s^{-1}. To avoid domain overlapping in the FEM modeling, a very small gap was introduced between the mounting plate and the plate-valve. Due to the meshing requirements, it is not possible to model the setup without the gap. The value for the air gap (h_d = 0.4 mm) was chosen iteratively to match the experimental results.
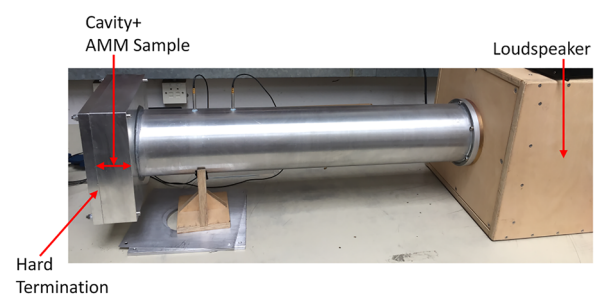

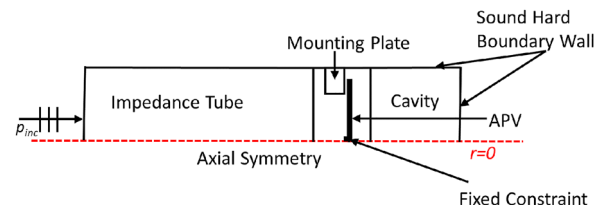**FIG. 15.** Photograph of the experimental test section with an impedance tube.

FIG. 16. Simplified 2D axisymmetric geometric model for numerical simulation.
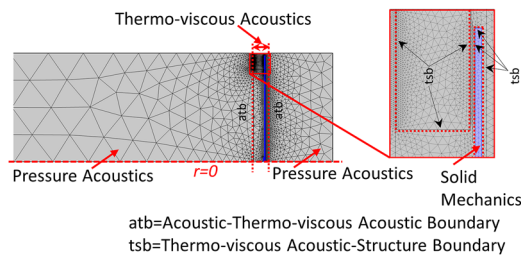
FIG. 17. Mesh plot of the simplified 2D axisymmetric geometric model for numerical simulation.

The complete mesh consists of 9688 domain elements and 880 boundary elements. The number of degrees of freedom solved for is 33 040. A parametric frequency sweep was performed from 50 to 1500 Hz with a 1 Hz frequency increment for frequency domain analysis. The average simulation time was 18 min 45 s on a workstation with the following specifications: an 8-core 2.40 GHz processor and 64 GB RAM.

In addition, an eigenfrequency analysis was also performed using only the solid mechanics part of the model for the acoustic plate-valve in order to obtain its structural resonance modes. The free vibration of the acoustic plate-valve (considered as a centrally fixed thin circular plate) *in vacuo* was investigated using this eigenfrequency analysis (for further details, see Appendix B). The meshing and the calculations of the reflection and absorption coefficient are demonstrated in the following sections.

a. Meshing

A user-controlled mesh with free triangular elements was used to create the mesh. The acoustic mesh element size criterion depends on the smallest acoustic wavelength (λ_0) of interest. Considering that the largest acoustic mesh element should never be larger than $\frac{1}{6}$ of the wavelength λ_0, the maximum and minimum element size are defined as $\frac{c_0}{6f_0}$ and $d_{visc}/3 = \frac{1}{3}\sqrt{\left(\frac{2\mu}{\omega\rho_0}\right)} = 220~\mu m \cdot \frac{1}{3} \cdot \sqrt{\left(\frac{100~Hz}{f_0}\right)}$ respectively. Figure 17 shows a portion of the mesh plot and highlights some of the mesh features in the vicinity of the acoustic plate-valve.

b. Estimation of the reflection and absorption coefficient

The absorption coefficient can be obtained using the incident acoustic impedance, which can be written as

$$Z_{in} = \frac{\langle p_t \rangle}{\langle -v_z \rangle}, \tag{A3}$$

where p_t is the total acoustic pressure, v_z is the acoustic velocity in the vertical direction, and $\langle \cdot \rangle$ is an operator referring to the average on the top surface of the system. The total impedance of the whole system can be obtained using the impedance translation theorem[41] in the form of transfer impedance as

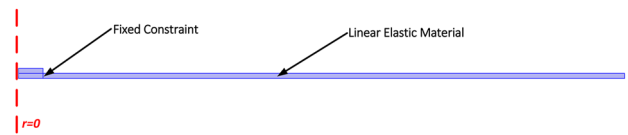$$Z_T = Z_0 \frac{Z_{in} + iZ_0 \tan(kL)}{Z_0 + iZ_{in} \tan(kL)}. \tag{A4}$$

FIG. 18. Linear elastic material model for eigenfrequency analysis.

Using the transfer impedance (Z_T), the reflection coefficient r has been obtained as

$$r = \frac{Z_T - Z_0}{Z_T + Z_0}, \tag{A5}$$

where $Z_0 = \rho_0 c_0$ is the specific acoustic impedance of the medium (i.e., air). Finally, the normal-incidence sound-absorption coefficient (α) is given by Eq. (A2).

APPENDIX B: EIGENFREQUENCY ANALYSIS

An eigenfrequency analysis provides the eigenfrequencies (natural frequencies) and mode shape (eigenmode) of a linear or linearized model. An eigenfrequency analysis has been performed using only the solid mechanics part of the model for the acoustic plate-valve to obtain the structural resonance modes according to the model shown in the schematic in Fig. 18. The eigenfrequency analysis was set to find the first 10 eigenfrequencies for symmetric modes. The physics-controlled mesh has been adapted for the model using a normal element size. To get the 10 desired number of eigenfrequencies around 50 Hz, the simulation run time was 2 s using the same workstation for frequency domain analysis.

The governing equation for the eigenfrequency analysis is

$$-\lambda_{mn} = i2\pi f_{mn} = i\omega_{mn}, \tag{B1}$$

where the fundamental eigenvalue is λ_{mn} and the eigenfrequency is f_{mn}. The eigenvalue problem without damping can be expressed as

$$\left[\mathbf{K} - \omega_{mn}^2\mathbf{M}\right]\mathbf{u} = 0, \tag{B2}$$

where $\mathbf{K}$ is the stiffness matrix, $\mathbf{M}$ is the mass matrix, and $\mathbf{u}$ is the eigenmode displacement vector. The eigenvalue problem with damping can be represented as

$$\left[\mathbf{K} + i\omega_{mn}\mathbf{C} - \omega_{mn}^2\mathbf{M}\right]\mathbf{u} = 0, \tag{B3}$$

where $\mathbf{C}$ is the viscous damping matrix and $\mathbf{K}$ can be complex valued.

REFERENCES

[1] S. Kumar and H. Lee, *Acoustics* (Multidisciplinary Digital Publishing Institute, 2019), Vol. 1, pp. 590–607.

[2] Y. Wang, K. Zhao, X.-Y. Lu, Y.-B. Song, and G. J. Bennett, Appl. Sci. **9**, 2224 (2019).

[3] K. Zhao, P. Okolo, E. Neri, P. Chen, J. Kennedy, and G. J. Bennett, Prog. Aerosp. Sci. **112**, 100589 (2019).

[4] J. Mei, G. Ma, M. Yang, Z. Yang, W. Wen, and P. Sheng, Nat. Commun. **3**, 756 (2012).

[5] C. Li, B. Cazzolato, and A. Zander, J. Acoust. Soc. Am. **139**, 93 (2016).

[6] K. Donda, Y. Zhu, S.-W. Fan, L. Cao, Y. Li, and B. Assouar, Appl. Phys. Lett. **115**, 173506 (2019).

[7] Y. Zhu, K. Donda, S. Fan, L. Cao, and B. Assouar, Appl. Phys. Express **12**, 114002 (2019).

[8] Y. Y. Lee, E. W. M. Lee, and C. F. Ng, J. Sound Vib. **287**, 227 (2005).

[9] C. Wang, L. Cheng, J. Pan, and G. Yu, J. Acoust. Soc. Am. **127**, 238 (2010).

[10] M. A. Temiz, J. Tournadre, I. Lopez Arteaga, and A. Hirschberg, Appl. Acoust. **125**, 80 (2017).

[11] E. Martincic, A. Houdouin, S. Durand, N. Yaakoubi, E. Lefeuvre, and Y. Auregan, "Acoustic absorber, acoustic wall and method for design and production," US Patent 10,477,302 (2019).

[12] A. McKay, I. Davis, J. Killeen, and G. J. Bennett, Sci. Rep. **10**, 17967 (2020).

[13] I. Davis, A. McKay, and G. J. Bennett, J. Sound Vib. **505**, 116135 (2021).

[14] J. Killeen, I. Davis, J. Wang, and G. J. Bennett, Appl. Acoust. **203**, 109229 (2022).

[15] J. Wang and G. J. Bennett, J. Sound Vib. **547**, 117527 (2023).

[16] M. Farooqui and Y. Aurégan, in *2018 AIAA/CEAS Aeroacoustics Conference* (AIAA, 2018), p. 4101.

[17] M. E. D'elia, T. Humbert, and Y. Aurégan, Acta Acust. **5**, 31 (2021).

[18] Y. Aurégan and M. Farooqui, Sci. Rep. **9**, 11140 (2019).

[19] G. J. Bennett, R. Hossain, A. McKay, and E. P. Ross, in *25th AIAA/CEAS Aeroacoustics Conference* (AIAA, 2019), p. 2422.

[20] H.-Y. Chiang and Y.-H. Huang, Appl. Acoust. **129**, 365 (2018).

[21] S. Timoshenko, W. Weaver, and D. Young, *Vibration Problems in Engineering* (John Wiley & Sons, 1928), c 1928, 1937, by d.

[22] R. V. Southwell, Proc. R. Soc. London, Ser. A **101**, 133 (1922).

[23] R. C. Colwell and H. C. Hardy, London, Edinburgh Dublin Philos. Mag. J. Sci. **24**, 1041 (1937).

[24] A. W. Leissa, *Vibration of Plates* (Scientific and Technical Information Division, National Aeronautics and Space Administration, 1969), Vol. 160.

[25] N. McLachlan, Proc. Phys. Soc. **44**, 546 (1932).

[26] R. W. Guy and M. C. Bhattacharya, J. Sound Vib. **27**, 207 (1973).

[27] J. Pan and D. A. Bies, J. Acoust. Soc. Am. **87**, 691 (1990).

[28] J. Pan and D. A. Bies, J. Acoust. Soc. Am. **87**, 708 (1990).

[29] D. G. Gorman, J. M. Reese, J. Horácek, and K. Dedouch, Proc. Inst. Mech. Eng., Part C **215**, 1303 (2001).

[30] D. G. Gorman, C. K. Lee, J. M. Reese, and J. Horáček, J. Sound Vib. **279**, 601 (2005).

[31] C. Rajalingham, R. B. Bhat, and G. D. Xistris, Int. J. Mech. Sci. **40**, 723 (1998).

[32] L. Yuanqi, L. Wang, Z. Shen, and Y. Tamura, J. Wind Eng. Ind. Aerodyn. **99**, 815 (2011).

[33] H. Liu, D. A. Olson, and M. Yu, J. Sound Vib. **333**, 7051 (2014).

[34] A. Presas, D. Valentin, E. Egusquiza, C. Valero, M. Egusquiza, and M. Bossio, Sensors **17**, 660 (2017).

[35] BS EN ISO 15034-2:2001, "Acoustics—Determination of sound absorption coefficient and impedance in impedance tubes—Part 2: Transfer-function method," Technical Standard BS EN ISO 15034-2:2001, British Standard, 2002.

[36] ASTM E2611-09, "Standard test method for measurement of normal incidence sound transmission of acoustical materials based on the transfer matrix method," Tech. Rep. ASTM E2611-09, ASTM International, 2009.

[37] T. Cox and P. d'Antonio, *Acoustic Absorbers and Diffusers: Theory, Design and Application* (CRC Press, 2016).

[38] J. Gietl, J. Vignola, J. Sterling, and T. Ryan, J. Phys.: Conf. Ser. **1149**(1), 012002 (2018).

[39] S. Mirkhalaf and M. Fagerström, Mech. Time-Depend. Mater. **25**, 119 (2021).

[40] K. Arunprasath, M. Vijayakumar, M. Ramarao, T. G. Arul, S. Peniel Pauldoss, M. Selwin, B. Radhakrishnan, and V. Manikandan, Mater. Today: Proc. **50**, 1559 (2022).

[41] B. E. Anderson and S. D. Sommerfeldt, J. Acoust. Soc. Am. **150**, 4155 (2021).